

Contents lists available at ScienceDirect

Earth and Planetary Science Letters

www.elsevier.com/locate/epsl



High pressure-temperature single-crystal elasticity of ringwoodite: Implications for detecting the 520 discontinuity and metastable ringwoodite at depths greater than 660 km



Wen-Yi Zhou ^{a,b,*}, Jin S. Zhang ^{a,b,*}, Quancheng Huang ^c, Xiaojing Lai ^{d,e}, Bin Chen ^e, Przemyslaw Dera ^e, Brandon Schmandt ^a

- ^a Department of Earth and Planetary Sciences, University of New Mexico, Albuquerque, NM, USA
- ^b Institute of Meteoritics, University of New Mexico, Albuquerque, NM, USA
- ^c Department of Physics, New Mexico State University, Las Cruces, NM, USA
- ^d Gemmological Institute, China University of Geosciences, Wuhan, Hubei, China
- ^e Hawaii Institute of Geophysics and Planetology, University of Hawaiʻi at Mānoa, Honolulu, HI, USA

ARTICLE INFO

Article history: Received 6 October 2021 Received in revised form 30 November 2021 Accepted 24 December 2021 Available online 7 January 2022 Editor: J. Badro

Keywords: ringwoodite sound velocity mantle transition zone the 520 low velocity zone

ABSTRACT

The 520 km discontinuity (the 520) and the 660 km discontinuity (the 660) are primarily caused by the wadsleyite to ringwoodite and ringwoodite to bridgmanite + ferropericlase phase transitions, respectively. Global seismic studies show significant regional variations of the 520, which are likely due to chemical and thermal heterogeneities in the Mantle Transition Zone (MTZ). However, the effects of chemical composition and temperature on the detectability of the 520 are unclear. Additionally, it remains unknown whether the possibly existing metastable ringwoodite in the core of the cold and fast subducting slabs could create a detectable seismic signature near the top of the lower mantle. Our understanding of both issues is hindered by the lack of single-crystal elasticity measurements of ringwoodite at simultaneous high pressure-temperature (P-T) conditions. In this study, we measured the single-crystal elasticity of an anhydrous Fe-bearing ringwoodite up to 32 GPa and 700 K by Brillouin spectroscopy, and then modeled the composition-dependent elastic properties of ringwoodite to calculate the compositional effects on the velocity jumps at the 520. We found that opposite to the effect of Fe, water enhances the Vp (P-wave velocity) jump, yet decreases the Vs (S-wave velocity) jump of the 520 across the wadsleyite to ringwoodite transition. Higher temperature increases both Vp and Vs contrasts across the 520. At depths between 660-700 km in the lower mantle, the existence of metastable ringwoodite may only result in \sim 1-2% low velocity anomaly, which is seismically difficult to resolve. The low velocity anomaly caused by metastable ringwoodite increases to 5-7% at 750 km depth due to the weak pressure dependence of Vs in ringwoodite at lower mantle conditions, but whether it is seismically detectable depends on the extension of the regions in subducted slabs that are sufficiently cold to host metastable ringwoodite.

© 2021 Elsevier B.V. All rights reserved.

Contents

		luction
	2.1.	Sample synthesis and characterization
	2.2.	High P-T Brillouin spectroscopy experiments and data analysis
	2.3.	Modeling of effects of Fe# and water on the velocity jumps across the wadsleyite-ringwoodite transition
3.	Result	ts
	3.1.	Elasticity of the anhydrous Fe-bearing ringwoodite sample measured in this study
	3.2.	Intrinsic anisotropy of ringwoodite

^{*} Corresponding authors at: Department of Earth and Planetary Sciences, University of New Mexico, Albuquerque, NM, USA. E-mail addresses: zwy1993@unm.edu (W.-Y. Zhou), jinzhang@unm.edu (J.S. Zhang).

4.	Discus	sion and	implications	6
	4.1.	Effects of	of Fe#, water, and temperature on velocity and impedance jumps of the 520	6
		4.1.1.	Effects of Fe# and water on Vp and Vs jumps at the 520	6
		4.1.2.	Effects of Fe# and water on Vp and Vs impedance jumps at the 520	8
		4.1.3.	Effect of temperature on the 520	8
			ble olivine and metastable ringwoodite	
			ntribution statement	
			ing interest	
Ackno	wledge	ment		9
Appen	dix A.	Supple	mentary material	10
Refere	nces			10

1. Introduction

The high pressure-temperature (P-T) phase transformations of olivine ((Mg, Fe)₂SiO₄) are largely responsible for 3 major seismic discontinuities in the Earth's ambient (normal) mantle: the 410 km seismic discontinuity (the 410), which separates the upper mantle and the mantle transition zone (MTZ), is linked to the olivine to wadsleyite transition; the wadsleyite to ringwoodite transformation corresponds to the 520 km seismic discontinuity (the 520); and finally the breakdown of ringwoodite to bridgmanite + ferropericlase marks the 660-km seismic discontinuity (the 660), which is the boundary between the MTZ and the lower mantle (Ringwood, 1991). While the 520 is believed to be a global feature (Tian et al., 2020), it is a less prominent discontinuity compared to the 410 and the 660. The depth and magnitude of the 520 (476-543 km, 1.2-4.8% velocity jump) vary significantly on a global scale, which is likely caused by chemical and thermal heterogeneities in the MTZ (Tian et al., 2020; Sinogeikin et al., 2003). The MTZ is a potential water reservoir due to the high water solubility in the structures of wadsleyite and ringwoodite as hydroxyl groups, but the water distribution in the MTZ is suggested to be highly variable based on global magnetotelluric and seismic studies (0-1 wt% water, e.g., Kelbert et al., 2009; Wang et al., 2021). However, the effect of water on the magnitude of the 520 (velocity and impedance contrasts) remains poorly constrained, particularly in the more realistic Fe-bearing system. A prior study by firstprinciples calculations modeled the effect of water in the Fe-free system and suggested that water reduces Vp and Vs impedance contrasts at the 520 (Panero, 2010). Sinogeikin et al. (2003) suggested that Fe enhances Vp and Vs velocity contrasts across the wadsleyite-ringwoodite transition, which was later contradicted by a first-principals computational study (Núñez-Valdez et al., 2011). Jacobsen and Smyth (2006) found that Vp of hydrous and anhydrous ringwoodite is indistinguishable under lower MTZ pressures at 300 K, while Mao et al. (2012) found that adding 1 wt% water into ringwoodite structure would significantly decrease both Vp and Vs by $\sim 2.5\%$ under similar P-T conditions. In addition, large discrepancies in terms of the high P-T single-crystal elastic properties of ringwoodite exist between the first-principles computational results and different experimental measurements (e.g., Mao et al., 2012; Schulze et al., 2018; Wang et al., 2021). The lack of benchmark high P-T single-crystal elasticity measurements on Fe-bearing ringwoodite has hindered quantitative efforts to resolve these existing discrepancies, as well as the further evaluation of the compositional and thermal effects on the detectability of the

It is worth noting that the transition pressures between olivine polymorphs in the Earth's interior, which largely control the 410, 520, and 660 depths, depend on the temperatures and Clapeyron slopes of these phase transitions. For example, the positive Clapeyron slope of the olivine-wadsleyite-ringwoodite transition would

result in shallower 410 and 520 under cold subduction zones, and a shallower 660 is expected under the deeply sourced hotspots due to the negative Clapeyron slope of ringwoodite to bridgmanite + ferropericlase transition (Lebedev et al., 2003). Compared with wadsleyite, olivine and ringwoodite have much larger thermodynamic stability fields in the composition-P-T space. Moreover, considering the transition kinetics, for cold and fast subducting slabs, when the descending rate of the slab is faster than the phase transition rate, low-pressure polymorphs may metastably exist at greater depth exceeding their pressure stability fields (Hosova et al., 2005). Seismic studies have identified low-velocity metastable olivine wedges in the core of the slabs subducting underneath Japan and Marianas at 410-560 km and 410-630 km depth ranges, respectively (Jiang et al., 2008; Kawakatsu and Yoshioka, 2011; Kaneshima et al., 2007). Ringwoodite may also metastably exist in the coldest part of the fast subducting slabs at depths greater than 660 km (Liu et al., 2018). However, due to the lack of knowledge on the sound velocities of metastable ringwoodite at relevant P-T conditions, whether metastable ringwoodite can be seismically detected remains unknown.

To overcome the aforementioned limitations, in this study, we measured single-crystal elasticity of an anhydrous Fe-bearing ringwoodite sample up to 32 GPa and 700 K by Brillouin spectroscopy. We then modeled the thermal and chemical effects on the magnitude of the 520 based on this study and literature data. We finally calculated the seismic properties of metastable ringwoodite near the 660 and discussed whether it might be detected in cold and fast subducting slabs.

2. Methods

2.1. Sample synthesis and characterization

San Carlos olivine was ground into powder and then packed in a boron nitride capsule without water in a 10/5 multi-anvil assembly to synthesize anhydrous Fe-bearing ringwoodite single crystals. The synthesis experiment was conducted at 1673 K and 18 GPa for 6.5 hours in a 1000-ton Multi-Anvil Press at the University of Hawai'i at Mānoa (UHM). The typical sizes of ringwoodite single crystals in the run product range from 30 µm to 90 µm. A few crystals \sim 70-90 μm in size were hand-picked and double-side polished into platelets with \sim 30-50 μm thickness and then examined using the Thermo Fisher Nicolet Nexus 670 Fourier Transformed Infrared Spectrometer (FTIR) with an infrared light source, a CaF₂ beam splitter, and a narrow-band mercury-cadmium-telluride detector at the University of New Mexico (UNM). We could not identify any visible peaks between 2400-3800 cm⁻¹ in the collected unpolarized FTIR spectra related with O-H in ringwoodite, suggesting that the synthetic ringwoodite crystals were nearly anhydrous. Typical FTIR spectra are shown in Fig. S1. We also determined the chemical composition of the synthetic ringwoodite crystals to be

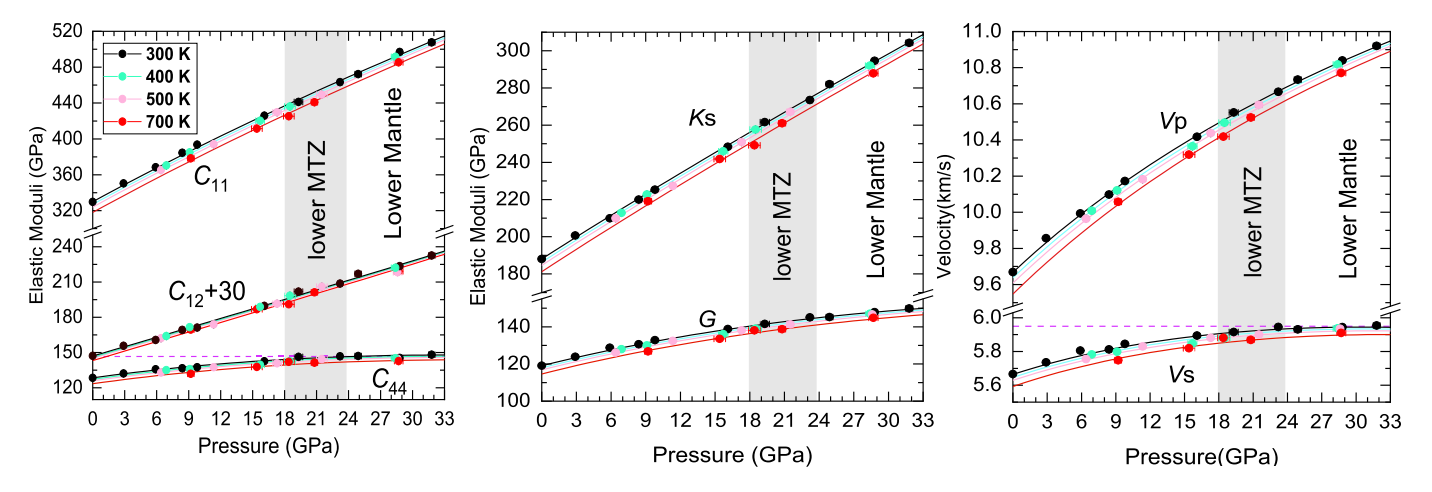


Fig. 1. C_{11} , C_{12} , C_{44} , K_{5} , G_{7} , V_{9} , and V_{5} of the Fe-bearing anhydrous ringwoodite measured in this study as a function of P_{7} along 300 K, 400 K, 500 K, 700 K isotherms (error bars are behind symbols). VRH averaging scheme is used to calculate the K_{5} , V_{7} , and V_{7} of the isotropic polycrystalline ringwoodite. Solid lines represent P_{7} induced increases of P_{7} and P_{7} are negligible above 23 GPa. (For interpretation of the colors in the figure(s), the reader is referred to the web version of this article.)

 $(Mg_{0.904}Fe_{0.096})_2SiO_4$ (Fe# = 9.60(3)) using the JEOL 8200 Electron Microprobe operated at 15 kV and 20 nA at UNM (Table S1). The major element standards were forsterite for Mg and Si, almandine for Fe and Al, and diopside for Ca.

We further polished 1 ringwoodite platelet down to \sim 10 µm thickness for single-crystal X-ray diffraction (XRD) and Brillouin spectroscopy experiments. The single-crystal XRD experiments were conducted under room *P-T* conditions at the X-ray Atlas Diffraction Lab using the Incoatec I μ S 3.0 AgK α microfocus source and a customized Bruker D8 Venture diffractometer at UHM. The diffraction images were collected in the φ -scan geometry for a φ angle range of \pm 23° with 1° step and 20-second exposure per frame. The unit cell parameters and crystal orientation were calculated using the Bruker APEX3 software. The density (ρ 0) at room *P-T* conditions was determined to be 3.709 (1) g/cm³ with the cubic unit cell parameter α = 8.0704 (6) Å. The plane normal of the ringwoodite platelet is determined to be (-0.8729, -0.4364, 0.2182).

2.2. High P-T Brillouin spectroscopy experiments and data analysis

We used a resistively heated BX90 diamond anvil cell (DAC) with 350 μm-culet diamond anvils to generate high P-T conditions for the Brillouin spectroscopy experiments (Kantor et al., 2012). The acoustically fast and slow directions of both diamond anvils were pre-determined using Brillouin spectroscopy based on the frequency shifts in the collected Brillouin spectra. The two diamond anvils were then manually rotated within the diamond anvil cell to ensure that their slow directions matched each other before experiments. A 250 um thick Rhenium gasket was indented to \sim 49 µm thickness, and a 250 µm hole was drilled at the center of the gasket to form the sample chamber. The polished ringwoodite platelet and 2 ruby spheres (pressure marker, Shen et al., 2020; Datchi et al., 2007) were loaded into the sample chamber. Neon was gas-loaded as the pressure-transmitting medium in the sample chamber at the GeoSoilEnviroCARS, Advanced Photon Source, Argonne National Laboratory. High temperature up to 700 K was generated by a platinum resistive heater placed around the diamond anvils in the BX90 DAC (Lai et al., 2020). We attached 2 K-type thermocouples near the diamond culet to determine the temperatures. The temperature differences given by the 2 thermocouples were always less than 15 K up to the maximum temperature reached during the experiments.

We conducted Brillouin spectroscopy experiments using 50° symmetric forward scattering geometry at the Laser Spectroscopy Laboratory at UNM. The light source is a single-mode 532 nm

solid-state laser. A 6-pass tandem Fabry-Pérot interferometer was used to measure the Brillouin frequency shift. The scattering angle of the Brillouin spectroscopy system was routinely calibrated using a standard silica glass Corning 7980 (Zhang et al., 2015). The scattering angles were calibrated twice during the 4-month experiments: 50.77° and 50.51°. We collected Brillouin spectra of ringwoodite with a step of 15° from Chi angle 0° to 360° at each P-T condition. Fig. S2 shows a typical Brillouin spectrum. Fewer velocity data were obtained at pressures higher than \sim 18 GPa (Fig. S3), because the ringwoodite v_p peaks start to overlap with the diamond v_s peaks along the acoustically slowest directions of diamonds. In addition, the externally connected electric wires of the heater sometimes blocked the scattered light path. At higher P-T conditions, bending the fragile heating wires back and forth can easily result in heater failure. Thus, we skipped the Brillouin measurements at Chi angles of 135° and 150° (Fig. S3). Fortunately, due to the high symmetry of ringwoodite, v_p and v_s along 8-10 different crystallographic directions are enough to constrain the 3 independent Ciis of ringwoodite. All the high P-T data are collected along the isotherms, respectively (Fig. 1). Typical collection time for a Brillouin spectrum with similar quality as the one shown in Fig. S2 is about 15-20 min at 300 K, and that reduces to about 10-15 min under high temperatures. The temperature averaged from the two thermocouple readings was stabilized at the target temperature of 400 K, 500 K, or 700 K during the high P-T experiments through adjustment of the heater power. The temperature fluctuations in each experimental run are less than 10 K.

With the initially estimated high P-T densities (Nishihara et al., 2004) and the measured phonon direction- v_p - v_s data set for ringwoodite, we inverted the best-fit C_{ii} s (C_{11} , C_{44} , C_{12}) under each P-T condition using Christoffel equation. The RMS errors are always less than 40 m/s, suggesting an excellent fit between the Ciis model and the measured velocities (Fig. S3). Voigt-Reuss-Hill (VRH) averaging scheme is used to calculate bulk modulus (Ks), shear modulus (G), Vp, and Vs for isotropic polycrystalline ringwoodite (Hill, 1963). Note the Vp and Vs are independent of the assumed densities, thus they are the true values at high P-T conditions. After fixing the Ks_0 , G_0 , ρ_0 , and thermal expansivity (Inoue et al., 2004), we fitted the P-T-Vp-Vs data set collected in this study using temperature-dependent 4th order finite strain equation of state (EOS) (Equations S1-S15, S19-S21) and derived the aggregate thermoelastic parameters: $(\partial K s/\partial P)_{T0}$, $(\partial^2 K s/\partial P^2)_{T0}$. $(\partial G/\partial P)_{T0}$, $(\partial^2 G/\partial P^2)_{T0}$, $(\partial Ks/\partial T)_{P0}$, $(\partial G/\partial T)_{P0}$, and best-fit high P-T densities (Davies and Dziewonski, 1975; Duffy and Anderson, 1989). We chose 4th order finite strain EOS here for fitting

Table 1 C_{ij} s, Ks, G, Vp, and Vs for the ringwoodite sample measured in this study.

Temperature	Pressure	density	C ₁₁	C ₄₄	C ₁₂	Ks	G	Vp	Vs
(K)	(GPa)	(g/cm ³)	(GPa)	(GPa)	(GPa)	(GPa)	(GPa)	(km/s)	(km/s)
300	0	3.709(1)	330(1)	128.5(6)	117(1)	188(1)	119 (1)	9.67(1)	5.67(1)
300	2.9(1)	3.765	350(1)	132.2(5)	126(1)	200.6(5)	123.9(7)	9.86(1)	5.74(1)
300	5.9(1)	3.820	369(1)	135.7(6)	131(1)	209.9(6)	128.7(6)	9.99(1)	5.81(1)
300	8.4(2)	3.865	384(1)	136.7(6)	139(1)	220.0(6)	130.6(5)	10.10(1)	5.81(1)
300	9.8(1)	3.889	393.6(9)	137.5(5)	141.2(9)	225.3(5)	132.9(4)	10.17(1)	5.84(1)
300	16.1(1)	3.994	426.0(7)	142.6(4)	159.6(6)	248.4(3)	138.8(3)	10.42(1)	5.89(1)
300	19.3(4)	4.044	441(1)	146.3(7)	172(1)	261.6(6)	141.5(5)	10.55(1)	5.92(1)
300	23.2(2)	4.104	463(1)	146.9(8)	179(1)	273.5(7)	145.0(4)	10.67(1)	5.95(1)
300	24.9(3)	4.129	472.3(1)	147.0(5)	187(1)	282.1(6)	145.2(3)	10.73(1)	5.93(1)
300	28.8(2)	4.186	497(1)	145.4(6)	194(1)	294.6(6)	147.9(4)	10.84(1)	5.94(1)
300	31.8(3)	4.228	508(1)	148.1(9)	203(1)	304.3(7)	149.9(5)	10.92(1)	5.95(1)
400	6.9(1)	3.828	370.3(9)	135.0(5)	134.0(9)	212.8(5)	128.0(5)	10.01(1)	5.78(1)
400	9.1(1)	3.867	385(1)	135.9(5)	141.6(9)	222.7(5)	130.0(5)	10.12(1)	5.80(1)
400	15.7(4)	3.977	420(1)	139.6(7)	159(1)	245.9(6)	136.0(4)	10.36(1)	5.85(1)
400	18.5(5)	4.022	436(1)	142.6(6)	168(1)	257.6(6)	139.0(4)	10.50(1)	5.88(1)
400	28.4(4)	4.170	492(2)	145.2(6)	192(2)	292.0(8)	147.0(4)	10.82(1)	5.94(1)
500	6.4(2)	3.808	365(1)	132.9(5)	132.2(9)	209.9(5)	126.1(5)	9.96(1)	5.76(1)
500	11.4(2)	3.895	394(1)	137.5(5)	143.9(9)	227.3(5)	132.4(4)	10.18(1)	5.83(1)
500	17.3(1)	3.993	430(1)	140.9(8)	161.5(1)	250.9(7)	138.1(5)	10.44(1)	5.88(1)
500	21.5(3)	4.058	449(1)	144.5(6)	176(1)	267.1(7)	141.3(4)	10.59(1)	5.90(1)
500	28.6(2)	4.164	488(1)	144.7(7)	188(1)	288.1(6)	146.6(4)	10.78(1)	5.93(1)
700	9.2(3)	3.837	378(1)	131.9(6)	140(1)	219.1(6)	126.8(5)	10.06(1)	5.75(1)
700	15.4(5)	3.942	411.5(9)	137.8(5)	156.9(8)	241.8(4)	133.5(4)	10.32(1)	5.82(1)
700	18.4(5)	3.991	425(1)	142.1(4)	161(1)	249.1(6)	138.0(3)	10.42(1)	5.88(1)
700	20.7(3)	4.027	440.9(9)	141.3(9)	171(1)	261.1(6)	138.7(5)	10.52(1)	5.87(1)
700	28.7(4)	4.146	485(1)	142.7(5)	189(1)	287.9(6)	144.8(4)	10.77(1)	5.91(1)

the aggregate elastic properties of ringwoodite instead of 3^{rd} order finite strain EOS due to the significantly reduced RMS error (12 m/s versus 44 m/s). As shown in Fig. S4, the use of 3^{rd} order finite strain EOS underestimates the Vp and Vs at lower pressures while overestimates them at higher pressures (23-32 GPa, Fig. 1). $C_{ij}s$, K_S , and G at each high P-T condition were then updated with the newly derived best-fit densities (Table 1). Finally, using temperature-dependent 3^{rd} order or 4^{th} order finite strain EOS (Equations S16-S18) (Davies, 1974; Duffy and Anderson, 1989), we fitted the P-T- $C_{ij}s$ data set to derive the pressure and temperature derivatives of the $C_{ij}s$: $(\partial C_{ij0}/\partial P)_{T0}$, $(\partial^2 C_{ij0}/\partial P^2)_{T0}$, $(\partial C_{ij0}/\partial T)_{P0}$ (Fig. 1; Table S2).

2.3. Modeling of effects of Fe# and water on the velocity jumps across the wadsleyite-ringwoodite transition

We adopted a similar procedure as what has been used in Zhou et al. (2021) to model the effects of Fe# $(\frac{100 \text{ Fe}_{mol}}{Mg_{mol}+Fe_{mol}})$ and water on the Vp and Vs of ringwoodite under high P-T conditions:

- (1) We compiled the water content, Fe#, density, Ks, G, Vp, and Vs of 8 different ringwoodite samples used in previous Brillouin spectroscopy studies (Jackson et al., 2000; Sinogeikin et al., 2003; Wang et al., 2006; Schulze et al., 2018, this study) to avoid any possible discrepancies resulting from the use of different experimental techniques, such as ultrasound interferometry. These ringwoodite samples cover a wide range of water content (0-2.34 wt%) and Fe# (0-11.5) (Fig. S5).
- (2) We fitted the ρ_0 , Ks_0 , G_0 of ringwoodite with respect to water contents (in wt%) and Fe# for these 8 different samples assuming an empirical linear relationship as shown in Table S3.
- (3) After adopting the results derived in step (2) under room *P-T* conditions, we fitted the parameters of the 4th order finite strain EOS to the entire Fe#, water and pressure-dependent Vp and Vs data set for the 8 ringwoodite samples to get water content and Fe# dependent $(\partial Ks/\partial P)_{T0}$, $(\partial^2 Ks/\partial P^2)_{T0}$, $(\partial G/\partial P)_{T0}$, and $(\partial^2 G/\partial P^2)_{T0}$ (Equations S1-S15, Table S3).

To evaluate the goodness of the fit of the obtained composition dependent high-pressure elasticity model, we compared the model-predicted values of Vp and Vs for all 8 ringwoodite samples with the experimentally determined values under high-pressure conditions. The differences are all within 1% for both Vp and Vs (Fig. S5A), suggesting our model is robust within the investigated range of water content and Fe# of ringwoodite in the Earth's mantle.

(4) Water content and Fe# in ringwoodite are suggested to have negligible effects on the temperature derivatives of Ks and G of ringwoodite (Schulze et al., 2018; Jackson et al., 2000; Sinogeikin et al., 2003). Therefore, we adopted $(\partial Ks/\partial T)_{P0}$ and $(\partial G/\partial T)_{P0}$ determined for the anhydrous Fe-bearing ringwoodite sample in this study in our model to calculate the high P-T elasticity of ringwoodite.

Combined with the composition-dependent high P-T elasticity model of wadsleyite in Zhou et al. (2020, 2021), we calculated the effects of water and Fe# on the velocity (Vp, Vs) as well as impedance contrasts across the wadsleyite-ringwoodite transition at 18 GPa along a 1600 K adiabat (Katsura et al., 2010). The impedance refers to density*velocity, the velocity and impedance jumps at the 520 for wadsleyite-ringwoodite phase transition are calculated as:

$$\frac{A \, (ringwoodite) - A \, (wadsleyite)}{A \, (ringwoodite) + A \, (wadsleyite)} * 200\% \tag{1}$$

where A is velocity or impedance. The water partitioning coefficient between wadsleyite and ringwoodite adopted in our modeling is 2:1 (Inoue et al., 2010). The Fe partitioning coefficient between wadsleyite and ringwoodite used in our modeling is 0.6 (Tsujino et al., 2019).

We would like to point out that in our model, we have included all previous single-crystal Brillouin spectroscopy studies of ringwoodite after 2000 except Mao et al. (2012). We excluded the experimental data in Mao et al. (2012) in our modeling based on the following reasons:

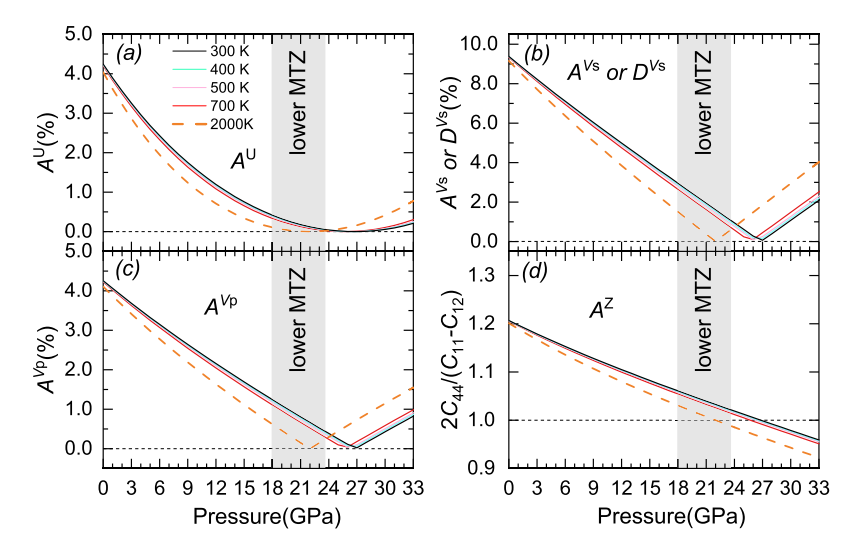


Fig. 2. Universal anisotropy (a), acoustic velocity anisotropy (b, c), and Zener anisotropy (d) of the Fe-bearing ringwoodite measured in this study as a function of pressure along different temperature isotherms

(1) We have computed another composition-dependent elasticity model of ringwoodite without excluding the data presented in Mao et al. (2012), as shown in Fig. S5B. However, the final best-fit model we obtained this way still shows large deviations from the data in Mao et al. (2012), while at the same time it fits the rest of the data in all the other studies well.

(2) Although the ringwoodite samples used in Schulze et al. (2018) and Mao et al. (2012) are compositionally very similar, the Vp and Vs obtained in Schulze et al. (2018) are \sim 2% and \sim 3% higher than what were presented in Mao et al. (2012), respectively. Our model is in excellent agreement with all the other experimental studies, including Schulze et al. (2018). As suggested by Schulze et al. (2018), the ringwoodite sample used in Mao et al. (2012) was possibly hydrated through a mechanism that is different from all the other studies. While we could not rule out the possibility that both potential hydration mechanisms may take place in nature, due to the lack of experimental data on the ringwoodite crystals hydrated through similar mechanisms as the sample used in Mao et al. (2012), we could only conduct the modeling work in this study based on all the other Brillouin spectroscopy studies. More sophisticated modeling work could be done with more experimental data available in the future.

3. Results

3.1. Elasticity of the anhydrous Fe-bearing ringwoodite sample measured in this study

The single-crystal elasticity measurements conducted in this study suggest that the 3 C_{ij} s (C_{11} , C_{44} , C_{12}) of ringwoodite behave differently with temperature and pressure (Fig. 1). C_{11} of ringwoodite is most sensitive to temperature while C_{12} is least sensitive (Fig. 1; Table S2). C_{11} is also most sensitive to pressure while C_{44} is least sensitive (Fig. 1), consistent with all previous studies for ringwoodite (Fig. S6, e.g., Sinogeikin et al., 2003; Wang et al., 2006, 2021; Mao et al., 2012; Schulze et al., 2018). C₁₁ and C_{12} increase almost linearly with pressure throughout the entire pressure range we investigated. In comparison, C₄₄ increases nonlinearly only up to \sim 23 GPa in this study, consistent with Schulze et al. (2018) as shown in Fig. S6. At pressures between 23 GPa and 32 GPa, C₄₄ remains almost constant, which has not been reported before due to the limited pressure range explored in previous studies. The weak pressure dependence of C_{44} possibly reflects the coupling between shear strains and atomic displacements in minerals with spinel-type structure (Caracas and Banigan, 2009).

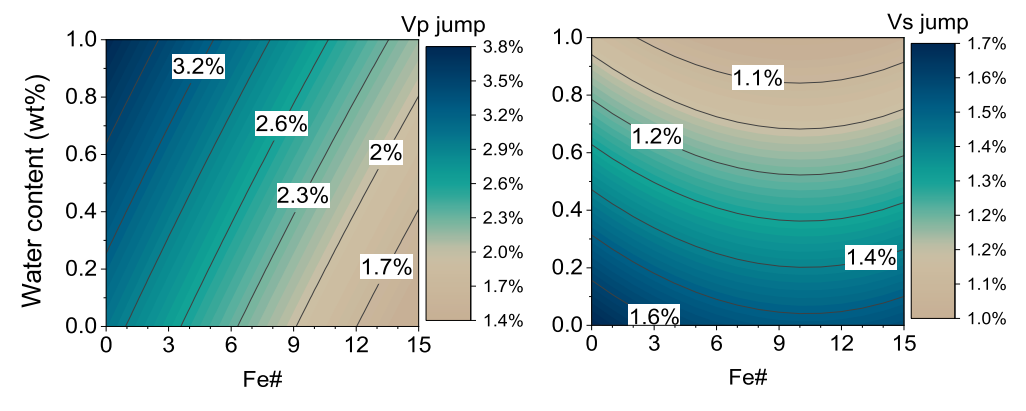
The elastic properties of an isotropic polycrystalline aggregate of ringwoodite are calculated under the VRH averaging scheme (Table 1). Vp increases with P from 0 GPa to 32 GPa, while the Vs increase becomes negligible when P exceeds \sim 23 GPa, mainly due to the minimal increase of C_{44} in the relevant pressure range (Fig. 1). The best-fit aggregate elastic properties for the anhydrous Fe-bearing ringwoodite sample used in this study are: $Ks_0 = 188$ (1) GPa, $G_0 = 119$ (1) GPa, $(\partial K s / \partial P)_{T0} = 4.0$ (2), $(\partial^2 K s / \partial P^2)_{T0}$ = -0.03 (2) GPa^{-1} , $(\partial G/\partial P)_{T0} = 1.56$ (7), $(\partial^2 G/\partial P^2)_{T0} = -$ 0.049 (6) GPa^{-1} , $(\partial K s/\partial T)_{P0} = -0.017$ (3) GPa/K, and $(\partial G/\partial T)_{P0}$ = -0.011 (2) GPa/K. Fixing the $(\partial^2 K s/\partial P^2)_{TO}$ to 0 GPa⁻¹ as what was done in previous studies (Mao et al., 2012; Schulze et al., 2018) yields slightly smaller $(\partial K s/\partial T)_{PO}$ (-0.014 (3) GPa/K) and $(\partial G/\partial T)_{P0}$ (-0.012 (2) GPa/K). The values of $(\partial K s/\partial T)_{P0}$ and $(\partial G/\partial T)_{PO}$ obtained in this study are in between the previous high P-T ultrasonic experiments on polycrystalline ringwoodite up to 18 GPa 1600 K ($(\partial K s/\partial T)_{P0} = -0.0181$ (8) GPa/K and $(\partial G/\partial T)_{P0} =$ - 0.0150 (4) GPa/K) by Higo et al. (2008), and previous high P-T XRD experiments up to 21 GPa 1273 K $((\partial Ks/\partial T)_{P0} = -0.008$ (5) GPa/K calculated from $(\partial K_T/\partial T)_{P0} = -0.015$ (5) GPa/K using Equation S24) by Nishihara et al. (2004) (Table S4).

3.2. Intrinsic anisotropy of ringwoodite

Based on the P-T dependence of the C_{ij} s measured in this study (Table S2), we calculated ringwoodite's intrinsic anisotropy indices under high P-T conditions (Fig. 2). A total of 5 elastic anisotropy indices are used: universal anisotropy (A^U), Zener anisotropy (A^Z), Vp azimuthal anisotropy (A^{Vp}), Vs azimuthal anisotropy (A^{Vs}), and Vs radial anisotropy (D^{Vs}) (see Equations S25-S29 and references in the Supplementary Information). For ringwoodite, due to its cubic symmetry, its A^{Vs} is equal to D^{Vs} (Fig. 2b).

The most prominent feature in Fig. 2 is that the intrinsic anisotropy of ringwoodite decreases significantly with pressure down to the bottom of the MTZ and then increases with pressure again. The increases of A^U , A^{Vp} , A^{Vs} and D^{Vs} above a certain threshold (e.g., \sim 27 GPa at 300 K) are the consequence of the switch between the acoustically fastest and the slowest crystallographic directions in ringwoodite, which is characterized by the decrease of A^Z below 1 (Fig. 2d, Table S5). Temperature also decreases the intrinsic anisotropy of Fe-bearing ringwoodite at the MTZ pressures, similar to Fe-free ringwoodite as suggested by previous first-principles calculations (Li et al., 2006). Previous stud-

A. Under 18GPa and 300K



B. Under 18GPa along 1600 K adiabatic geotherm

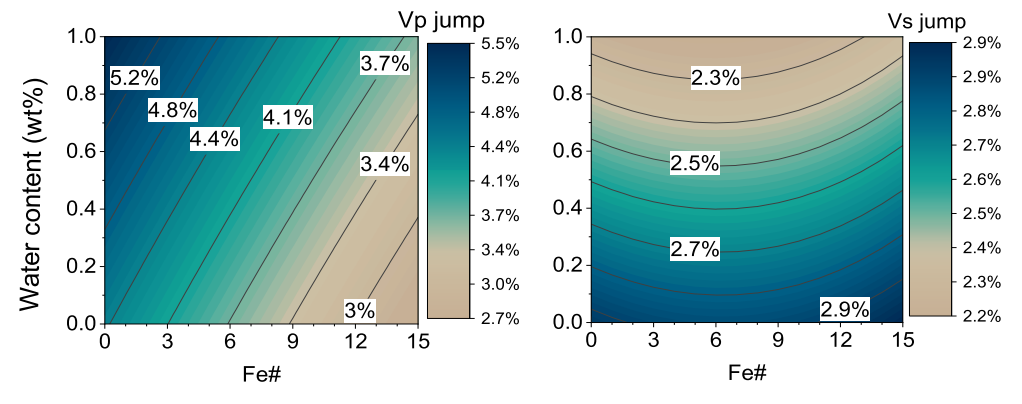


Fig. 3. Effects of Fe# and water on the Vp and Vs jumps (Equation (1)) across the wadsleyite-ringwoodite transition in pure (Mg, Fe)₂SiO₄ system. The horizontal axis is the Fe# in ringwoodite ($Fe\#_{ring}$), the corresponding Fe# in wadsleyite is $\frac{60Fe\#_{ring}}{(100-0.4Fe\#_{ring})}$ according to the Fe partitioning coefficient of 0.6 between wadsleyite and ringwoodite (Tsujino et al., 2019). The vertical axis is the water content in ringwoodite, 1 wt% of water in ringwoodite corresponds to 2 wt% of water in wadsleyite based on the water partitioning coefficient of 2 between wadsleyite and ringwoodite (Inoue et al., 2010).

ies suggested that the intrinsic elastic anisotropy of ringwoodite is small (e.g., Wang et al., 2006; Schulze et al., 2018). At lower MTZ conditions, our study suggests that Fe-bearing ringwoodite is elastically almost isotropic with all 4 elastic anisotropy indices approaching 0. Note, these values represent the maximum possible seismic anisotropy that can be induced by the lattice preferred orientations (LPO) of ringwoodite. The realistic seismic anisotropy induced by LPO of ringwoodite would be significantly less, thus any observed seismic anisotropy in the lower MTZ (e.g., Zhang et al., 2021) is unlikely to be caused by the presence of ringwoodite. Minerals with significantly higher elastic anisotropy (e.g., akimotoite, stishovite, metastable olivine) or shape-preferred orientation of rheologically/elastically weak minerals melts are the more possible explanations for the observed seismic anisotropy in the MTZ (Zhou et al., 2021 and references in Zhou et al., 2021).

4. Discussion and implications

4.1. Effects of Fe#, water, and temperature on velocity and impedance jumps of the 520

Based on the experimental data of ringwoodite measured in this study and previous studies (Fig. S5A), we modeled the effects of water content and Fe# on the elasticity of ringwoodite under high *P-T* conditions (Table S3). Combined with a previous composition-dependent elasticity model of wadsleyite under high *P-T* conditions (Zhou et al., 2020, 2021), we evaluated the effects of Fe#, water, and temperature on the velocity and impedance jumps across the wadsleyite to ringwoodite transition in pure (Mg, Fe)₂SiO₄ system (Figs. 3, 4). In the Earth's mantle, these jumps

would be smaller considering the dilution effect due to the coexistence of garnet. Assuming the Earth's mantle is pyrolitic with $\sim\!53$ vol% olivine, based on the phase equilibrium experiments by Ishii et al. (2018), the 520 for a pyrolitic MTZ is characterized by $\sim\!2\%$ $V\,\mathrm{p}$ and $V\,\mathrm{s}$ velocity jumps as well as $\sim\!3\%$ $V\,\mathrm{p}$ and $V\,\mathrm{s}$ impedance jumps with a theoretical thickness of 0 km. Our results agree with the globally estimated $\sim\!3\%$ $V\,\mathrm{p}$ and $V\,\mathrm{s}$ impedance contrasts across the 520 of using SS precursors by Shearer (1990). It is worth noting that, for SS precursors studies, a strong trade-off exists between the impedance contrast and sharpness of the 520. As pointed by Tian et al. (2020), a 0-km thick 520 with $V\,\mathrm{s}$ impedance contrast of 2.4% can result in the same waveform as a 30-km wide 520 with 4.4% $V\,\mathrm{s}$ impedance contrast.

4.1.1. Effects of Fe# and water on Vp and Vs jumps at the 520

The effects of Fe# and water on the velocity jumps across wadsleyite-ringwoodite transition are shown in Fig. 3. Increasing Fe# reduces the Vp jump. Fe increases the $(\partial Ks/\partial P)_{T0}$ of wadsleyite (Buchen et al., 2017; Zhou et al., 2021), whereas the $(\partial Ks/\partial P)_{T0}$ of ringwoodite is not sensitive to Fe# (Table 2, Higo et al., 2006). The Ks of wadsleyite approaches that of ringwoodite with increasing Fe# in both wadsleyite and ringwoodite. Interestingly, the Vs jump is less sensitive to Fe (Fig. 3), because the effect of Fe on Vs jump is controlled by 2 competing factors. On the one hand, wadsleyite's V_S and G are more sensitive to Fe compared with ringwoodite (e.g., adding 1 mol% of Fe decreases wadsleyite's G_0 by 0.5% and ringwoodite's G_0 by only 0.2%), and thus, adding the same amount of Fe in wadsleyite and ringwoodite could enhance the Vs jump. On the other hand, Fe# of ringwoodite is larger than Fe# of wadsleyite under equilibrated mantle condi-

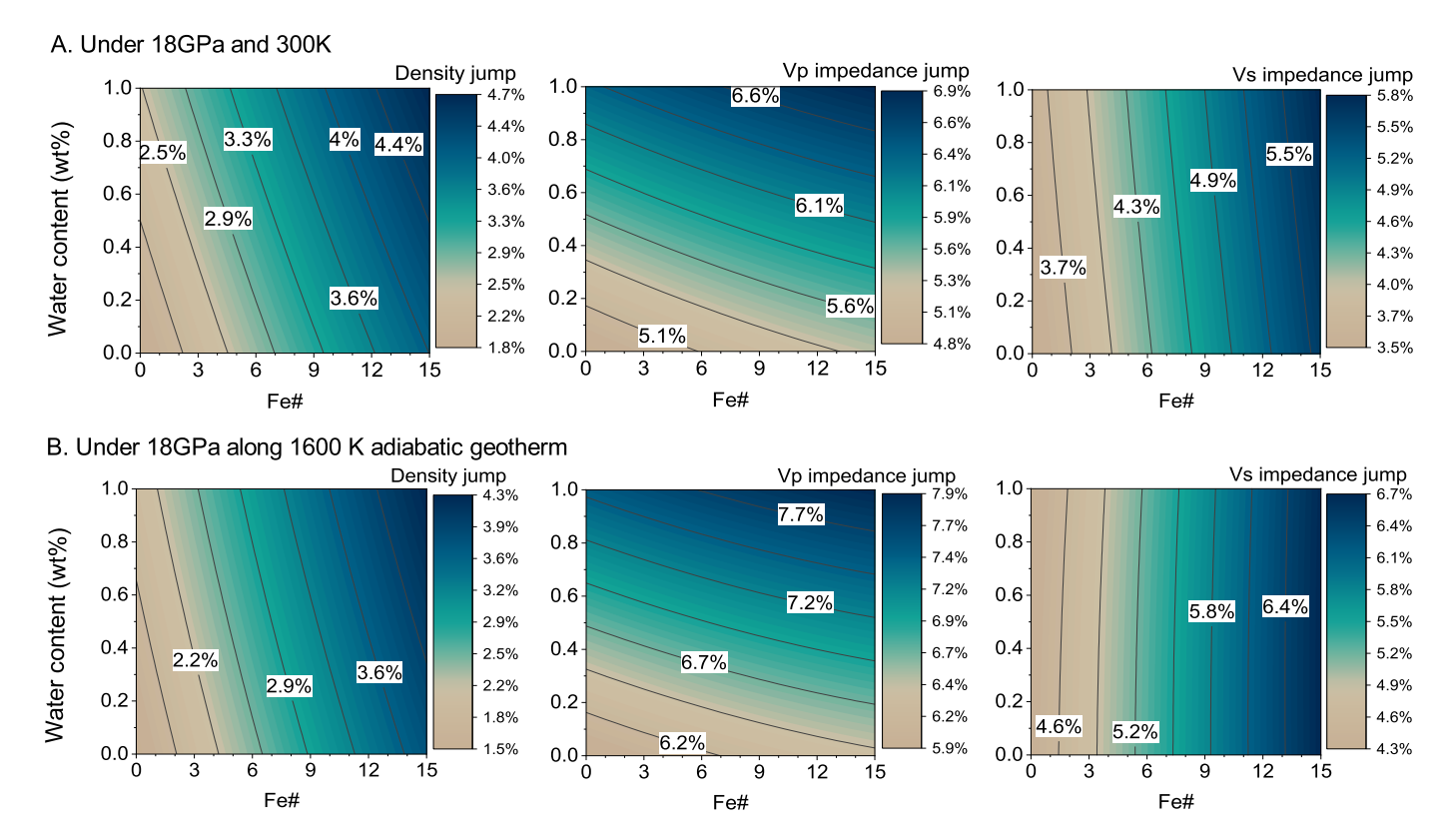


Fig. 4. Effects of Fe# and water on density, Vp impedance contrast and Vs impedance contrast (Equation (1)) across wadsleyite-ringwoodite transition in pure (Mg, Fe)₂SiO₄ system. The horizontal axis is the Fe# in ringwoodite ($Fe#_{ring}$), the corresponding Fe# in wadsleyite is: $Fe#_{wad} = \frac{60Fe#_{ring}}{1000-0.4Fe#_{ring}}$ based on the average Fe partitioning coefficient of 0.6 between wadsleyite and ringwoodite (Tsujino et al., 2019). The vertical axis is the water content in ringwoodite. 1 wt% of water in ringwoodite corresponds to 2 wt% of water in wadsleyite based on the water partitioning coefficient of 2 between wadsleyite and ringwoodite (Inoue et al., 2010).

Table 2Comparison of the effects of water content and Fe# on the elastic properties of wadsleyite (Zhou et al., 2020, 2021) and ringwoodite (this study).

	Wadsleyite		Ringwoodite			
	Increase Fe# by 1	Add 1 wt% water	Increase Fe# by 1	Add 1 wt% water		
Ks ₀	\	↓ by 4%	↑ by 0.1%	↓ by 5%		
$(\partial K s/\partial P)_{TO}$	↑ by 1.3%	\	\	↑ by 5%		
$(\partial K s/\partial T)_{P0}$	\	\	\	\		
G_0	↓ by 0.5%	↓ by 5%	↓ by 0.1%	↓ by 5%		
$(\partial G/\partial P)_{T0}$	\	↑ by 10%	\	↑ by 7%		
$(\partial^2 G/\partial P^2)_{T0}$	\	\	\	\		
$(\partial G/\partial T)_{P0}$	\	\	\	\		

tion considering Fe preferentially partitions into ringwoodite (e.g. 2 mol% of Fe in ringwoodite corresponds to \sim 1.2 mol% Fe in wadsleyite) (Tsujino et al., 2019), increasing Fe# in the MTZ could reduce the Vs jump across the wadsleyite-ringwoodite transition.

Sinogeikin et al. (2003) suggested that higher Fe content will increase both the Vp and Vs jumps across the 520 primarily based on the elasticity measurements at ambient condition, whereas Núñez-Valdez et al. (2011) suggested the opposite based on first-principles calculations. Our results (the Vp jump is reduced by Fe whereas the Vs jump is almost insensitive to Fe) are in partial agreement with both studies. Sinogeikin et al. (2003) assumed that Fe does not affect $(\partial Ks/\partial P)_{T0}$ of wadsleyite while our calculation adopted the relationship that was determined in Zhou et al. (2021), which suggested that adding 1 mol% Fe increases the $(\partial Ks/\partial P)_{T0}$ of wadsleyite by 1.3%. This relationship is in agreement with Buchen et al. (2017) which also found that Fe increases the $(\partial K_T/\partial P)_{T0}$ of wadsleyite. On the other hand, Núñez-Valdez et al. (2011) suggested Fe of ringwoodite decreases its $(\partial G/\partial P)_{T0}$ and finally decreases Vs jump at the 520, while our result (Table 2)

shows that Fe has no resolvable effect on $(\partial G/\partial P)_{T0}$ of ringwoodite. Our result, in terms of the Fe effect on the $(\partial G/\partial P)_{T0}$ and $(\partial K_T/\partial P)_{T0}$ of ringwoodite, is consistent with Higo et al. (2006).

In contrast to the effect of Fe, higher water content increases Vp jump across the wadsleyite to ringwoodite transition at the 520. Higher water content increases $(\partial Ks/\partial P)_{T0}$ of ringwoodite (Jacobsen and Smyth, 2006), whereas $(\partial Ks/\partial P)_{T0}$ of wadsleyite is not sensitive to water content (Table 2). Thus, the difference between the Vp of ringwoodite and wadsleyite increases with water content (Fig. 3). On the other hand, water reduces the Vs jump across the wadsleyite to ringwoodite transition. Adding 1 wt% water into the crystal structures increases $(\partial G/\partial P)_{T0}$ of wadsleyite and ringwoodite by 10% and 7%, respectively (Table 2). Moreover, considering the water preferably partitions into wadsleyite than ringwoodite (Inoue et al., 2010), incorporating twice as much water in wadsleyite than ringwoodite would results in an even higher $(\partial G/\partial P)_{T0}$ of the hydrous wadsleyite coexisting with the hydrous ringwoodite near the 520. As a result, wadsleyite's G or Vs ap-

proaches those of ringwoodite at 18 GPa with increasing water content in the MTZ.

4.1.2. Effects of Fe# and water on Vp and Vs impedance jumps at the 520

The density and impedance jumps across the wadsleyiteringwoodite transition at the 520 are shown in Fig. 4. Fe increases the densities of both ringwoodite and wadsleyite, but the density of ringwoodite is more sensitive to Fe. Moreover, Fe preferentially partitions into ringwoodite compared with wadsleyite (Tsujino et al., 2019). Thus, increasing Fe# of the MTZ increases the density jump across the wadsleyite to ringwoodite transition (Fig. 4). Similarly, increasing water content in the MTZ would result in an increase of the density jump at the 520, because water preferentially partitions into wadsleyite rather than ringwoodite and water decreases densities of both ringwoodite and wadsleyite (Inoue et al., 2010). Due to the influence of density, V p impedance contrast is more sensitive to water and less sensitive to Fe compared with Vp jump, whereas Vs impedance contrast is much more sensitive to Fe and less sensitive to water compared with Vs jump (Figs. 3, 4).

4.1.3. Effect of temperature on the 520

To understand the influence of temperature on the 520, we calculated the velocity jumps and impedance contrasts across the wadsleyite to ringwoodite transition at 18 GPa along a 1600 K adiabat (Katsura et al., 2010) and compared with the results at 18 GPa and 300 K (Figs. 3, 4). Temperature strongly enhances all velocity jumps while it decreases density jump, and thus, temperature only weakly enhances the impedance (density*velocity) contrasts across the wadsleyite to ringwoodite. Our results are different from the first-principles calculation studies in the Fe-free system (Yonggang et al., 2008; Panero, 2010). Yonggang et al. (2008) suggested that temperature has a negligible effect on the 520 impedance contrasts, whereas Panero (2010) suggests that temperature decreases the 520 impedance contrasts for Fe-free olivine polymorphs.

In summary, Fe, water, and temperature have different effects on Vp and Vs jumps across the wadsleyite-ringwoodite transformation at the 520. Fe decreases the Vp jump and is insensitive to the Vs jump. Water increases the Vp jump yet decreases the Vs jump. Temperature increases both Vp and Vs jumps. The mineral physics modeling in this study suggests that lateral changes in chemical composition and temperature in the MTZ can help explain the global variations of the 520. In addition, our findings have potential applications in estimating water content in the MTZ. For example, in a hydrated MTZ, we would expect a slightly higher Vp jump with a reduced Vs jump across the 520. However, the hydration effect needs to be used with caution, since local variation of Fe# could also influence the observed magnitude of the 520.

4.2. Metastable olivine and metastable ringwoodite

Due to the transition kinetics, metastable olivine and ringwoodite may survive at depths greater than 410 km and 660 km, respectively, under P-T conditions in cold subduction zones (Hosoya et al., 2005). A metastable olivine wedge has been reported beneath the Japan Sea at \sim 410-560 km depth range based on waveform modeling of the P-wave coda (e.g., Kaneshima et al., 2007), forward travel time modeling (e.g., Jiang et al., 2008), receiver functions (Kawakatsu and Yoshioka, 2011), and inter-source interferometry (Shen and Zhan, 2020). Kaneshima et al. (2007), Jiang et al. (2008), and Shen and Zhan (2020) all suggested that V p of the metastable olivine wedge beneath the Japan Sea is \sim 3% slower than the ambient mantle and \sim 5% slower than the surrounding slabs at 410-560 km. If this subducting slab remains relatively cold at the bottom

Pressure (GPa)

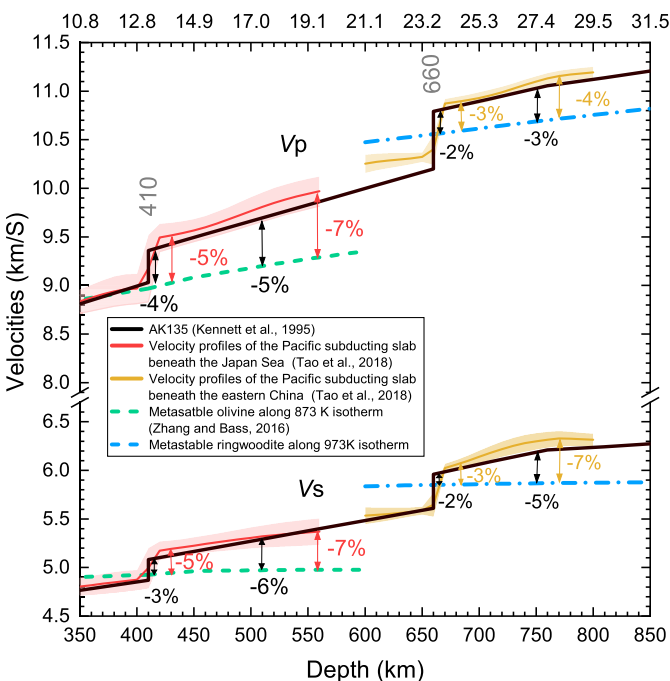


Fig. 5. Negative velocity anomaly caused by metastable olivine and ringwoodite compared with an ambient mantle (AK135) and the Pacific subducting slab beneath the Japan Sea and the eastern China, respectively. The shaded areas denote the standard deviations of Vp and Vs from the averaged velocities of the Pacific subducting slab under the Japan Sea and the eastern China. The velocity profiles of the Pacific subducting slab as a function of depth are based on the tomography study by Tao et al. (2018). They only represent the averaged velocity profiles of the slab, the thin metastable olivine or ringwoodite wedges inside the slab could not be resolved by seismic tomography in Tao et al. (2018).

of the MTZ (e.g., < 973 K, Inoue et al., 2004; Bina and Navrotsky, 2000), metastable ringwoodite may exist in the form of a low velocity wedge near the slab core extending from \sim 660 km to greater depth in the lower mantle (Liu et al., 2018), similar to the metastable olivine wedge in the MTZ. However, whether these wedge-shape slow anomaly caused by ringwoodite can be observed seismically remains unknown.

In this study, we modeled the seismic anomalies that are induced by metastable olivine and possibly metastable ringwoodite in the Pacific slab subducting underneath the Japan Sea and the eastern China using the mineral physics data in this study and previous study (Zhang and Bass, 2016). The velocity structure of an ambient mantle is represented by the global seismic model AK135 (Kennett et al., 1995). The Pacific subducting slab reaches the MTZ depths under the Japan Sea, and penetrates through the 660 beneath the eastern China (Tao et al., 2018). Therefore, the velocity structure of the Pacific subducting slab at 410-560 km depth is illustrated by the local seismic model under the Japan Sea (36°- 42° latitude and 130° - 140° longitude), whereas the local seismic model under the eastern China was used to show the slab's velocity structure at 660-800 km depth (30°-40° latitude and 115°-125°). We calculated Vp and Vs of anhydrous olivine (Fe#=9.5, Zhang and Bass, 2016) along an 873 K isotherm as well as the Vp and Vs of anhydrous ringwoodite (Fe#=9.6, this study) along a 973 K isotherm (Fig. 5). The metastable olivine and ringwoodite are assumed to be anhydrous. Ishii and Ohtani (2021) suggested that water strongly partitions into the high-pressure hydrous minerals (such as hydrous phase A) in wet subducting slabs, thus the nominally anhydrous olivine and its high-pressure polymorphs are nearly dry. We choose the 873 K isotherm for metastable olivine and the 973 K isotherm for metastable ringwoodite for the fol-

lowing reasons. Hosoya et al. (2005) suggested that at 873 K, nearly dry olivine (500 ppm water) could metastably exist down to the depth of \sim 650 km in the Earth's interior based on in-situ XRD DAC experiments. At 1 atm, anhydrous ringwoodite would not transform back to olivine until the temperature reaches 973 K (Inoue et al., 2004). At much higher pressures in the Earth's interior, the decomposition of ringwoodite into bridgmanite + ferropericlase is thus unlikely to take place as long as the temperature remains lower than 973 K. It is possible that olivine and ringwoodite can metastably survive at even higher temperature inside the Earth, thus 873 K and 973 K are conservative estimates of the temperatures that metastable olivine and ringwoodite can exist at depths greater than 410 km and 660 km, respectively. In addition, 873 K and 973 K are consistent with the modeled core temperature of the western Pacific subducting slabs in the MTZ (700-973 K) (Bina and Navrotsky, 2000; Kawakatsu and Yoshioka, 2011; Ishii and Ohtani, 2021).

As shown in Fig. 5, the Vp of olivine is about 5% lower than the ambient mantle (AK135) and 5-7% lower than the surrounding slabs under the Japan Sea at 410-560 km depths. These values are consistent with the observed Vp anomalies of the metastable olivine wedge (\sim 3% lower than the ambient mantle, \sim 5% lower than the nearby slabs) beneath the Japan Sea at 410-560 km depths considering that the lithospheric mantle of the subducting slabs contains \sim 60-80 vol% olivine (Shen and Zhan, 2020).

Whether metastable ringwoodite could cause seismically detectable low velocity regions at 660-700 km depends on both the volume of metastable ringwoodite in slabs and the velocity contrast between the metastable ringwoodite and mantle nearby. At the depth between 660-700 km, metastable ringwoodite is only \sim 2-3% slower than the ambient mantle (AK135) and the Pacific subducting slab beneath the eastern China. Considering the dilution effect caused by the coexistence of majoritic garnet (20-40 vol% garnet) in the subducted lithosphere, metastable ringwoodite wedge would only result in \sim 1-2% low velocity anomaly at the depth of 660-700 km, which may not be detectable.

However, metastable ringwoodite, if it exists, could produce a stronger negative Vs anomaly at greater depth due to the minimal increase of Vs with pressure at lower mantle conditions. For example, Vs of metastable ringwoodite would be \sim 5% slower than the ambient mantle (AK135) and \sim 7% slower than the Pacific subducting slab if it can reach \sim 750 km depth. Whether it is detectable also depends on the volume of metastable ringwoodite wedge in the subducting slabs. Kawakatsu and Yoshioka (2011) modeled the temperature distributions of the Pacific subducting slab stagnant at the 660 under Japan Sea. They found that the layer with T < T973 K near the core of the slab is <5 km thick at the 660. This layer might get thinner after it reaches even greater depth, making metastable ringwoodite wedge too thin to be resolved seismically although it carries a strong negative Vs anomaly at \sim 750 km. In comparison, the metastable olivine wedge in the subducting slab beneath the Japan Sea is observed to be \sim 30-50 km wide at 410 km depth, making it easier to resolve with seismic imaging (Jiang et al., 2008; Kawakatsu and Yoshioka, 2011; Shen and Zhan, 2020). If ringwoodite can metastably exist at slightly higher temperature at depths greater than 660 km, for example, 1173 K, then the thickness of the metastable ringwoodite wedge could reach ~25-30 km, making it more likely to be detected. Alternatively, if the slab folds and buckles near the 660, and thus has a thick cold core (e.g., Marianas region, Li et al., 2019), the layer enriched in metastable ringwoodite might also become seismically detectable as the low velocity layers near the top of the lower mantle.

In summary, different from a metastable olivine wedge, which carries a stronger seismic velocity anomaly, a metastable ringwoodite wedge, if it exists, is more likely to become seismically detectable with stronger Vs anomaly at depths greater than \sim 750

km if the cold core of the slab is sufficiently thick. Future studies on the metastability field of ringwoodite under subduction zone P-T conditions are needed to better understand the detectability of metastable ringwoodite.

5. Conclusions

- (1) We determined the elasticity of anhydrous Fe-bearing single-crystal ringwoodite (Fe# = 9.6) up to 32 GPa and 700 K by Brillouin Spectroscopy. The coefficients of the 4th order finite Eulerian strains equations describing the isotropic aggregate bulk and shear moduli of anhydrous ringwoodite (Fe# = 9.6) at high *P-T* conditions are: $Ks_0 = 188$ (1) GPa, $G_0 = 119$ (1) GPa, $(\partial Ks/\partial P)_{T0} = 4.0$ (2), $(\partial^2 Ks/\partial P^2)_{T0} = -0.03$ (2) GPa⁻¹, $(\partial G/\partial P)_{T0} = 1.56$ (7), $(\partial^2 G/\partial P^2)_{T0} = -0.049$ (6) GPa⁻¹, $(\partial Ks/\partial T)_{P0} = -0.017$ (3) GPa/K, and $(\partial G/\partial T)_{P0} = -0.011$ (2) GPa/K.
- (2) The intrinsic elastic anisotropy of ringwoodite is approaching 0 at the bottom of the MTZ. Lattice preferred orientation of ringwoodite could not account for the seismic anisotropy observed in the lower MTZ.
- (3) Fe, water, and temperature have different effects on Vp and Vs jumps across the wadsleyite-ringwoodite transformation. Fe decreases the Vp jump and is insensitive to the Vs jump. Water increases the Vp jump yet decreases the Vs jump. Temperature increases both Vp and Vs jumps. Lateral changes in chemical composition and temperature in the MTZ could help explain the strong global variations of the 520.
- (4) We calculated the sound velocity of metastable ringwoodite at depths greater than 660 km. Compared with a metastable olivine wedge in cold subducting slabs, seismic detection of a metastable ringwoodite wedge is challenging due to its smaller velocity contrast and lesser thickness. Future studies on the metastability field of ringwoodite under subduction zone *P-T* conditions are needed.

CRediT authorship contribution statement

Wen-Yi Zhou: Sample preparation, Data curation, Formal analysis, Visualization, Coding, Writing-original draft.

Jin S. Zhang: Methodology, Visualization, Coding, Supervision, Resources, Funding acquisition, Writing - review & editing.

Quancheng Huang: Validation, Writing - review & editing. Xiaojing Lai: Sample synthesis, Writing - review & editing. Bin Chen: Sample synthesis, Writing - review & editing.

Przemyslaw Dera: Sample characterization, Writing - review & editing.

Brandon Schmandt: Validation, Funding acquisition, Writing - review & editing.

Declaration of competing interest

The authors declare that they have no known competing financial interests or personal relationships that could have appeared to influence the work reported in this paper.

Acknowledgement

We thank Mingqiang Hou for help in sample preparation and Mike Splide for help in Electron Microprobe Analysis experiments at UNM. We thank Ruijia Wang for help in data analysis. We also thank Sergey Tkachev for the gas loading of the DACs at GSE-CARS, APS, ANL. The use of the gas-loading system is supported by COMPRES, the Consortium for Materials Properties Research in Earth Sciences under NSF Co-operative Agreement EAR 1661511,

and GSECARS is funded by National Science Foundation (NSF-EAR1634415) and Department of Energy (DOE) – GeoSciences (DE-FG02-94ER14466). This project is supported by NSF-EAR1664471 (J.S.Z and B.S).

Appendix A. Supplementary material

Supplementary material related to this article can be found online at https://doi.org/10.1016/j.epsl.2021.117359.

References

- Bina, C.R., Navrotsky, A., 2000. Possible presence of high-pressure ice in cold subducting slabs. Nature 408 (6814), 844–847. https://doi.org/10.1038/35048555.
- Buchen, J., Marquardt, H., Boffa Ballaran, T., Kawazoe, T., McCammon, C., 2017. The equation of state of wadsleyite solid solutions: constraining the effects of anisotropy and crystal chemistry. Am. Mineral.: J. Earth Planet. Mater. 102 (12), 2494–2504. https://doi.org/10.2138/am-2017-6162.
- Caracas, R., Banigan, E.J., 2009. Elasticity and Raman and infrared spectra of MgAl2O4 spinel from density functional perturbation theory. Phys. Earth Planet. Inter. 174 (1–4), 113–121. https://doi.org/10.1016/j.pepi.2009.01.001.
- Datchi, F., Dewaele, A., Loubeyre, P., Letoullec, R., Le Godec, Y., Canny, B., 2007. Optical pressure sensors for high-pressure-high-temperature studies in a diamond anvil cell. High Press. Res. 27 (4), 447–463. https://doi.org/10.1080/08957950701659593.
- Davies, G., 1974. Effective elastic moduli under hydrostatic stress—I. Quasi-harmonic theory. J. Phys. Chem. Solids 35, 1513–1520. https://doi.org/10.1016/S0022-3697(74)80279-9
- Davies, G., Dziewonski, A., 1975. Homogeneity and constitution of the Earth's lower mantle and outer core. Phys. Earth Planet. Inter. 10, 336–343. https://doi.org/10. 1016/0031-9201(75)90060-6.
- Duffy, T.S., Anderson, D.L., 1989. Seismic velocities in mantle minerals and the mineralogy of the upper mantle. J. Geophys. Res., Solid Earth 94, 1895–1912. https://doi.org/10.1029/IB094iB02p01895.
- Higo, Y., Inoue, T., Irifune, T., Funakoshi, K.I., Li, B., 2008. Elastic wave velocities of (Mg0. 91Fe0. 09) 2SiO4 ringwoodite under P-T conditions of the mantle transition region. Phys. Earth Planet. Inter. 166 (3-4), 167-174. https:// doi.org/10.1016/j.pepi.2008.01.003.
- Higo, Y., Inoue, T., Li, B., Irifune, T., Liebermann, R.C., 2006. The effect of iron on the elastic properties of ringwoodite at high pressure. Phys. Earth Planet. Inter. 159 (3–4), 276–285. https://doi.org/10.1016/j.pepi.2006.08.004.
- Hill, R., 1963. Elastic properties of reinforced solids: some theoretical principles. J. Mech. Phys. Solids 11, 357–372. https://doi.org/10.1016/0022-5096(63)90036-X.
- Hosoya, T., Kubo, T., Ohtani, E., Sano, A., Funakoshi, K.I., 2005. Water controls the fields of metastable olivine in cold subducting slabs. Geophys. Res. Lett. 32 (17). https://doi.org/10.1029/2005GL023398.
- Inoue, T., Tanimoto, Y., Irifune, T., Suzuki, T., Fukui, H., Ohtaka, O., 2004. Thermal expansion of wadsleyite, ringwoodite, hydrous wadsleyite and hydrous ringwoodite. Phys. Earth Planet. Inter. 143, 279–290. https://doi.org/10.1016/j.pepi. 2003.07.021.
- Inoue, T., Wada, T., Sasaki, R., Yurimoto, H., 2010. Water partitioning in the Earth's mantle. Phys. Earth Planet. Inter. 183 (1–2), 245–251. https://doi.org/10.1016/j. pepi.2010.08.003.
- Ishii, T., Kojitani, H., Akaogi, M., 2018. Phase relations and mineral chemistry in pyrolitic mantle at 1600–2200° C under pressures up to the uppermost lower mantle: phase transitions around the 660-km discontinuity and dynamics of upwelling hot plumes. Phys. Earth Planet. Inter. 274, 127–137. https://doi.org/10.1016/j.pepi.2017.10.005.
- Ishii, T., Ohtani, E., 2021. Dry metastable olivine and slab deformation in a wet subducting slab. Nat. Geosci., 1–5. https://doi.org/10.1038/s41561-021-00756-7.
- Jackson, J.M., Sinogeikin, S.V., Bass, J.D., 2000. Sound velocities and elastic properties of γ -Mg2SiO4 to 873 K by Brillouin spectroscopy. Am. Mineral. 85 (2), 296–303. https://doi.org/10.2138/am-2000-2-306.
- Jacobsen, S.D., Smyth, J.R., 2006. Effect of water on the sound velocities of ring-woodite in the transition zone. In: Jacobsen, S.D., Lee, S.V.D. (Eds.), Earth's Deep Water Cycle. American Geophysical Union, pp. 131–145.
- Jiang, G., Zhao, D., Zhang, G., 2008. Seismic evidence for a metastable olivine wedge in the subducting Pacific slab under Japan Sea. Earth Planet. Sci. Lett. 270 (3–4), 300–307. https://doi.org/10.1016/j.epsl.2008.03.037.
- Kaneshima, S., Okamoto, T., Takenaka, H., 2007. Evidence for a metastable olivine wedge inside the subducted Mariana slab. Earth Planet. Sci. Lett. 258, 219–227. https://doi.org/10.1016/j.epsl.2007.03.035.
- Kantor, I., Prakapenka, V., Kantor, A., Dera, P., Kurnosov, A., Sinogeikin, S., Dubrovinskaia, N., Dubrovinsky, L., 2012. BX90: a new diamond anvil cell design for X-ray diffraction and optical measurements. Rev. Sci. Instrum. 83 (12), 125102. https://doi.org/10.1063/1.4768541.
- Katsura, T., Yoneda, A., Yamazaki, D., Yoshino, T., Ito, E., 2010. Adiabatic temperature profile in the mantle. Phys. Earth Planet. Inter. 183 (1–2), 212–218. https://doi. org/10.1016/j.pepi.2010.07.001.

- Kawakatsu, H., Yoshioka, S., 2011. Metastable olivine wedge and deep dry cold slab beneath southwest Japan. Earth Planet. Sci. Lett. 303 (1–2), 1–10. https://doi.org/10.1016/j.epsl.2011.01.008.
- Kelbert, A., Schultz, A., Egbert, G., 2009. Global electromagnetic induction constraints on transition-zone water content variations. Nature 460 (7258), 1003–1006. https://doi.org/10.1038/nature08257.
- Kennett, B.L., Engdahl, E.R., Buland, R., 1995. Constraints on seismic velocities in the Earth from traveltimes. Geophys. J. Int. 122 (1), 108–124. https://doi.org/10. 1111/i.1365-246X.1995.tb03540.x.
- Lai, X., Zhu, F., Zhang, J.S., Zhang, D., Tkachev, S., Prakapenka, V.B., Chen, B., 2020. An externally-heated diamond anvil cell for synthesis and single-crystal elasticity determination of ice-VII at high pressure-temperature conditions. J. Vis. Exp. (160), e61389. https://doi.org/10.3791/61389.
- Lebedev, S., Chevrot, S., Van der Hilst, R.D., 2003. Correlation between the shear-speed structure and thickness of the mantle transition zone. Phys. Earth Planet. Inter. 136 (1–2), 25–40. https://doi.org/10.1016/S0031-9201(03)00020-7.
- Li, L., Weidner, D.J., Brodholt, J., Alfe, D., Price, G.D., 2006. Elasticity of Mg2SiO4 ringwoodite at mantle conditions. Phys. Earth Planet. Inter. 157 (3–4), 181–187. https://doi.org/10.1016/j.pepi.2006.04.002.
- Li, Z.-H., Gerya, T., Connolly, J.A., 2019. Variability of subducting slab morphologies in the mantle transition zone: insight from petrological-thermomechanical modeling. Earth-Sci. Rev. 196, 102874. https://doi.org/10.1016/j.earscirev.2019.05.018.
- Liu, Z., Park, J., Karato, S.I., 2018. Seismic evidence for water transport out of the mantle transition zone beneath the European Alps. Earth Planet. Sci. Lett. 482, 93–104. https://doi.org/10.1016/j.epsl.2017.10.054.
- Mao, Z., Lin, J.F., Jacobsen, S.D., Duffy, T.S., Chang, Y.Y., Smyth, J.R., et al., 2012. Sound velocities of hydrous ringwoodite to 16 GPa and 673 K. Earth Planet. Sci. Lett. 331, 112–119. https://doi.org/10.1016/j.epsl.2012.03.001.
- Nishihara, Y., Takahashi, E., Matsukage, K.N., Iguchi, T., Nakayama, K., Funakoshi, K.I., 2004. Thermal equation of state of (Mg0. 91Fe0. 09) 2SiO4 ringwoodite. Phys. Earth Planet. Inter. 143, 33–46. https://doi.org/10.1016/j.pepi.2003.02.001.
- Núñez-Valdez, M., Da Silveira, P., Wentzcovitch, R.M., 2011. Influence of iron on the elastic properties of wadsleyite and ringwoodite. J. Geophys. Res., Solid Earth 116 (B12). https://doi.org/10.1029/2011JB008378.
- Panero, W.R., 2010. First principles determination of the structure and elasticity of hydrous ringwoodite. J. Geophys. Res., Solid Earth 115 (B3). https://doi.org/10. 1029/2008/B006282.
- Ringwood, A.E., 1991. Phase transformations and their bearing on the constitution and dynamics of the mantle. Geochim. Cosmochim. Acta 55 (8), 2083–2110. https://doi.org/10.1016/0016-7037(91)90090-R.
- Schulze, K., Marquardt, H., Kawazoe, T., Ballaran, T.B., McCammon, C., Koch-Müller, M., et al., 2018. Seismically invisible water in Earth's transition zone? Earth Planet. Sci. Lett. 498, 9–16. https://doi.org/10.1016/j.epsl.2018.06.021.
- Shearer, P.M., 1990. Seismic imaging of upper-mantle structure with new evidence for a 520-km discontinuity. Nature 344, 121–126. https://doi.org/10.1038/344121a0
- Shen, G., Wang, Y., Dewaele, A., Wu, C., Fratanduono, D.E., Eggert, J., Klotz, S., Dziubek, K.F., Loubeyre, P., Fat'yanov, O.V., Asimow, P.D., 2020. Toward an international practical pressure scale: a proposal for an IPPS ruby gauge (IPPS-Ruby2020). High Press. Res. 40 (3), 299–314. https://doi.org/10.1080/08957959. 2020.1791107.
- Shen, Z., Zhan, Z., 2020. Metastable olivine wedge beneath the Japan Sea imaged by seismic interferometry. Geophys. Res. Lett. 47 (6), e2019GL085665. https:// doi.org/10.1029/2019GL085665.
- Sinogeikin, S.V., Bass, J.D., Katsura, T., 2003. Single-crystal elasticity of ringwoodite to high pressures and high temperatures: implications for 520 km seismic discontinuity. Phys. Earth Planet. Inter. 136 (1–2), 41–66. https://doi.org/10.1016/S0031-9201(03)00022-0.
- Tao, K., Grand, S.P., Niu, F.N., 2018. Seismic structure of the upper mantle beneath Eastern Asia from full waveform seismic tomography. Geochem. Geophys. Geosyst. https://doi.org/10.1029/2018GC007460.
- Tian, D., Lv, M., Wei, S.S., Dorfman, S.M., Shearer, P.M., 2020. Global variations of Earth's 520- and 560-km discontinuities. Earth Planet. Sci. Lett. 552, 116600. https://doi.org/10.1016/j.epsl.2020.116600.
- Tsujino, N., Yoshino, T., Yamazaki, D., Sakurai, M., Sun, W., Xu, F., Tange, Y., Higo, Y., 2019. Phase transition of wadsleyite-ringwoodite in the Mg2SiO4-Fe2SiO4 system. Am. Mineral.: J. Earth Planet. Mater. 104 (4), 588–594. https://doi.org/10.2138/am-2019-6823.
- Wang, J., Sinogeikin, S.V., Inoue, T., Bass, J.D., 2006. Elastic properties of hydrous ringwoodite at high-pressure conditions. Geophys. Res. Lett. 33 (14). https://doi. org/10.1029/2006GL026441.
- Wang, W., Zhang, H., Brodholt, J.P., Wu, Z., 2021. Elasticity of hydrous ringwoodite at mantle conditions: implication for water distribution in the lowermost mantle transition zone. Earth Planet. Sci. Lett. 554, 116626. https://doi.org/10.1016/j. epsl.2020.116626.
- Yonggang, G.Y., Wu, Z., Wentzcovitch, R.M., 2008. α-β-γ transformations in Mg2SiO4 in Earth's transition zone. Earth Planet. Sci. Lett. 273 (1–2), 115–122. https://doi.org/10.1016/i.epsl.2008.06.023.

- Zhang, J.S., Bass, J.D., 2016. Sound velocities of olivine at high pressures and temperatures and the composition of Earth's upper mantle. Geophys. Res. Lett. 43 (18), 9611–9618. https://doi.org/10.1002/2016GL069949.
- Zhang, J.S., Bass, J.D., Zhu, G., 2015. Single-crystal Brillouin spectroscopy with CO2 laser heating and variable q. Rev. Sci. Instrum. 86, 063905. https://doi.org/10. 1063/1.4922634.
- Zhang, H., Schmandt, B., Zhang, J.S., 2021. Localized anisotropy in the mantle transition zone due to flow through slab gaps. Geophys. Res. Lett. 48 (10), e2021GL092712. https://doi.org/10.1029/2021GL092712.
- Zhou, W.Y., Hao, M., Ohuchi, T., Chen, B., Miyagi, L.M., Schmandt, B., Zhang, J.S., 2020. Anisotropy of the Upper Mantle Transition Zone constrained from the first experimentally determined high temperature-pressure single-crystal elasticity data of wadsleyite. In: AGU Fall Meeting Abstracts, vol. 2020, p. DI030-07.
- Zhou, W.Y., Ren, Z., Zhang, J.S., Chen, B., Hao, M., Ohuchi, T., Miyagi, L., Zhang, D., Alp, E.E., Lavina, B., Schmandt, B., 2021. The Water-Fe-Pressure dependent single-crystal elastic properties of wadsleyite: implications for the seismic anisotropy in the upper Mantle Transition Zone. Earth Planet. Sci. Lett. 565, 116955. https://doi.org/10.1016/j.epsl.2021.116955.